ESTIMATION OF WALL SHEAR STRESS DYNAMIC FLUCTUATIONS IN INTRACRANIAL ATHEROSCLEROTIC LESIONS USING COMPUTATIONAL FLUID DYNAMICS

Clemens M. Schirmer, M.D.

Department of Neurosurgery, Cerebrovascular and Endovascular Division, Tufts Medical Center and Tufts University School of Medicine, Boston, Massachusetts

Adel M. Malek, M.D., Ph.D.

Department of Neurosurgery, Cerebrovascular and Endovascular Division, Tufts Medical Center and Tufts University School of Medicine, Boston, Massachusetts

Reprint requests:
Adel M. Malek, M.D., Ph.D., Department of Neurosurgery, Tufts Medical Center, 800 Washington Street, Suite 178, Boston, MA 02111.
Email: amalek@tuftsmedicalcenter.org

Received, October 28, 2007.
Accepted, April 18, 2008.



ONLINE DIGITAL VIDEO

OBJECTIVE: Intracranial stenosis (IS) is associated with significant morbidity and mortality from hypoperfusion and thromboembolism. We used computational fluid dynamic methods to analyze luminal patterns of wall shear stress (WSS), a known critical modulator of endothelial function, within patient-based IS lesions undergoing percutaneous angioplasty and stenting.

METHODS: High-resolution three-dimensional rotational angiographic data sets were reconstructed to yield a fine-resolution computational mesh allowing application of pulsatile computational fluid dynamic analysis with a non-Newtonian realistic model of blood. WSS and its gradient were analyzed spatiotemporally in five IS lesions before and after percutaneous angioplasty and stenting.

RESULTS: WSS within the stenosis reached average shear magnitudes of 1870 ± 783 dyn/cm^2 with rapidly reversing direction to oscillating low values in the recirculation zone. WSS vectors revealed complex dynamic directional and amplitude oscillations not seen in healthy segments with time-dependent convergence and divergence strips sweeping back and forth across the lesion during the cardiac cycle. These areas also underwent extreme temporal WSS oscillation of 2052 ± 909 dyn/cm^2 over a short time interval. The endothelial mechanotransductive response to such extreme WSS magnitudes and gradients, which were normalized by percutaneous angioplasty and stenting in the current study, remains undefined.

CONCLUSION: Computational fluid dynamic analysis of IS has uncovered a complex and hostile microhemodynamic environment characterized by wide and rapid shear variations in time and space. Characterization of the mechanical forces acting on the wall can help in determining the molecular transduction response of the luminal endothelium to these extreme stresses and may lead to better understanding of the hemodynamic contribution to stenosis pathophysiology.

KEY WORDS: Atherosclerosis, Endothelium, Fluid mechanics, Stenosis, Stenting

Neurosurgery 63:326–335, 2008 DOI: 10.1227/01.NEU.0000313119.73941.9E www.neurosurgery-online.com

Intracranial stenosis (IS) is a dynamic process associated with significant morbidity and mortality (1, 26). Although both medical treatment (27) and endovascular revascularization have been used to treat IS, the optimal treatment strategy remains unclear (12). Study of the contribution of hemodynamic forces in the multifactorial risk profile of IS (37) has been hampered by the location of the lesions and by the flow complexity introduced by the three-dimensional anatomy of the intracranial vasculature. Hemodynamic factors, including wall shear stress (WSS) resulting from the frictional force acting on the luminal vessel wall, are both established regulators of endothelial cell (EC) function and possible contributors to atherosclerosis (21, 23, 33). WSS changes in space and time, in addition to WSS magnitude, have been shown to affect EC function. WSS temporal gradients lead to ERK1/2 activation (4), increased EC proliferation (50), nitric oxide elaboration (3), and increased monocyte-to-EC adhesion (24), and spatial gradients lead to increased endothelial monolayer permeability (38), EC migration (45), and transcriptional factor activation (35).

Although computational fluid dynamic (CFD) analysis has been applied to theoretical stenoses, little is known about the

Abbreviations: CFD, computational fluid dynamic; **EC**, endothelial cell; **IS**, intracranial stenosis; **OSI**, oscillatory shear index; **PSR**, poststenotic region; **PTAS**, percutaneous angioplasty and stenting; **WSS**, wall shear stress

TABLE 1. Demographics and location of intracranial stenosis lesions treated using percutaneous angioplasty and stenting[a]

Patient	Age (yr)/ sex	Side	Vessel	Segment	SAH	Angiographic stenosis (%)[b]	Symptoms
1	49/F	L	ICA	Petrous ICA	No	72.5	Recent right ICA occlusion caused by supraclinoid stenosis, left ICA petrous stenosis
2	56/M	L	ICA	Petrous ICA	No	79	Recurrent TIA of right arm and face
3	69/M	R	ICA	Petrous ICA	No	79	Transient episode of hypotension during surgery, MRI revealed petrocavernous right ICA stenosis
4	55/M	R	ICA	Petrous ICA	No	82	Progressive visual symptoms and acute episode of decreased visual acuity in right eye
5	67/M	L	VBJ	VBJ	Yes	76	SAH, fusiform aneurysm of the left VA, distal intracranial and proximal intracranial left vertebral artery stenosis

[a] SAH, subarachnoid hemorrhage; L, left; ICA, internal carotid artery; TIA, transient ischemic attack; R, right; VBJ, vertebrobasilar junction; VA, vertebral artery; MRI, magnetic resonance imaging.
[b] Calculated using North American Symptomatic Carotid Endarterectomy Trial criteria (36).

spatial and temporal pattern of WSS within actual patient-based stenotic lesions, because of computational complexity (43, 46) and a lack of motion-free high-resolution data describing the three-dimensional geometry of atherosclerotic vessels. Although IS lesions are less accessible than their cervical counterparts, their fixed location within the bony confines of the cranial base enables the use of three-dimensional rotational angiography to obtain a high-resolution representation of the parent vessel and luminal anatomy.

Most biomechanical studies have centered on defining the pattern of blood flow within the stenotic vessel and have lacked adequate resolution to estimate WSS (7, 28). We sought CFD analysis to characterize the spectrum of wall shear forces in space and time within high-resolution patient IS geometries with a fine computational mesh and a realistic non-Newtonian Carreau-Yasuda formulation of blood viscosity. We examined lesions before and after percutaneous angioplasty and stenting (PTAS) to evaluate the latter's effect on restoring the intracranial hemodynamic milieu.

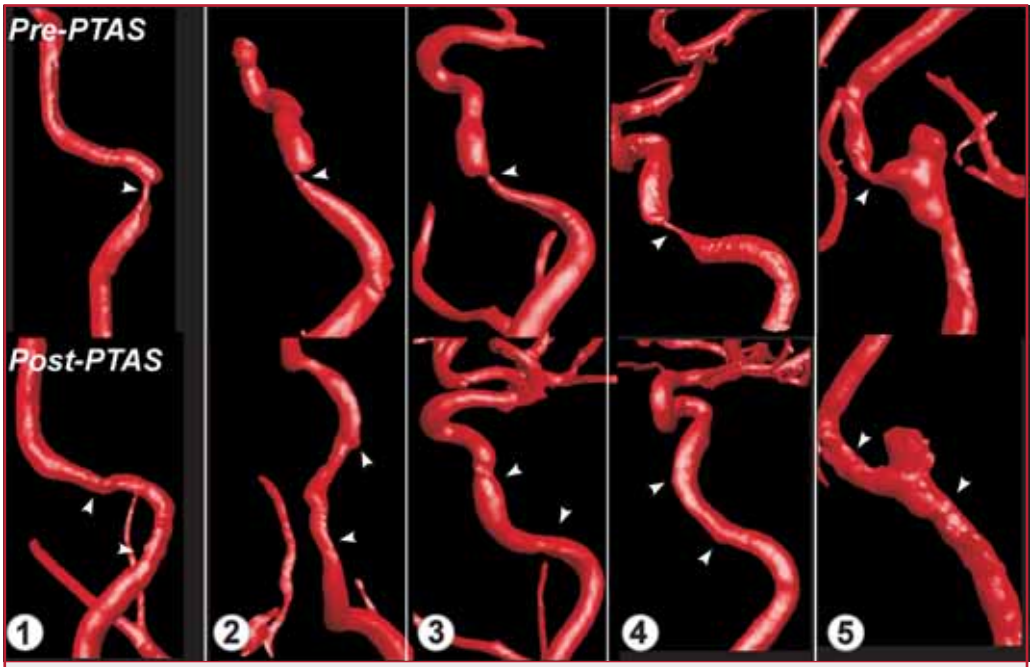


FIGURE 1. *Pre-percutaneous angioplasty and stenting* (Pre-PTAS) (arrowheads *point to the stenosis) and* Post-PTAS (arrowheads *show the location of the stent) three-dimensional rotational angiography models. Numbers reflect the numbering of the cases in* Table 1.

PATIENTS AND METHODS

Five patients with symptomatic intracranial atherosclerotic disease recalcitrant to medical therapy were selected to undergo PTAS. *Table 1* shows the demographics, presentation, and angiographic location and degree of stenosis of the patients in this study. Our methods have been previously described in detail (41). In summary, biplane digital subtraction angiography and three-dimensional rotational angiography were performed (Integris Allura; Philips Medical Systems, Andover, MA). Three-dimensional rotational angiography acquisitions were reconstructed into three-dimensional data sets (*Fig. 1*); surface renderings of the luminal anatomy of the IS lesion were generated as previously described and used to generate high-resolution predominantly hexahedral computational meshes (41, 42).

A laminar transient flow model was used for the simulation with a Carreau non-Newtonian formulation of the viscous properties of blood

(41, 42, 47, 48). Numerical computations were carried out using Fluent (Version 6.2.16; Fluent, Inc., Lebanon, NH) on a cluster of desktop computers. Pulsatile CFD was performed for three cardiac cycles, assuming a rigid vessel wall and nonslip and nonpenetration constraints at the wall.

The computational approach used in the current study has been previously validated (41) using available experimental data (2, 42). Lack of dependence on grid density, inlet boundary condition, and periodicity were established as described previously (41).

Postprocessing was performed using Ensight software (Version 8; Computational Engineering International, Apex, NC). The oscillatory shear index (OSI) was calculated as:

$$\mathrm{OSI} = \frac{1}{2}\left(1 - \frac{\left|\int_0^T \vec{\tau}_w dt\right|}{\int_0^T \left|\vec{\tau}_w\right| dt}\right)$$

where $\vec{\tau}_w$ is the instantaneous wall shear stress vector and T denotes the length of the pulse cycle (25). Statistical analysis of mean values was performed using Student's t tests and statistical significance was assumed for P values less than 0.05 (SAS Institute, Inc., Cary, NC).

RESULTS

Wall Shear Stress within Intracranial Stenosis Lesions

(see video at web site)

CFD analysis enabled the computation of the pulsatile shear stress vector including direction and magnitude on the luminal surface as a function of time (*Fig. 2A*; *Video 1*). All lesions were characterized by flow acceleration into the throat of the stenosis marked by rapid rise in WSS magnitude, followed at the distal stenosis by emergence of flow separation with development of a retrograde shear vector in the poststenotic region (PSR) and eventual distal flow reattachment.

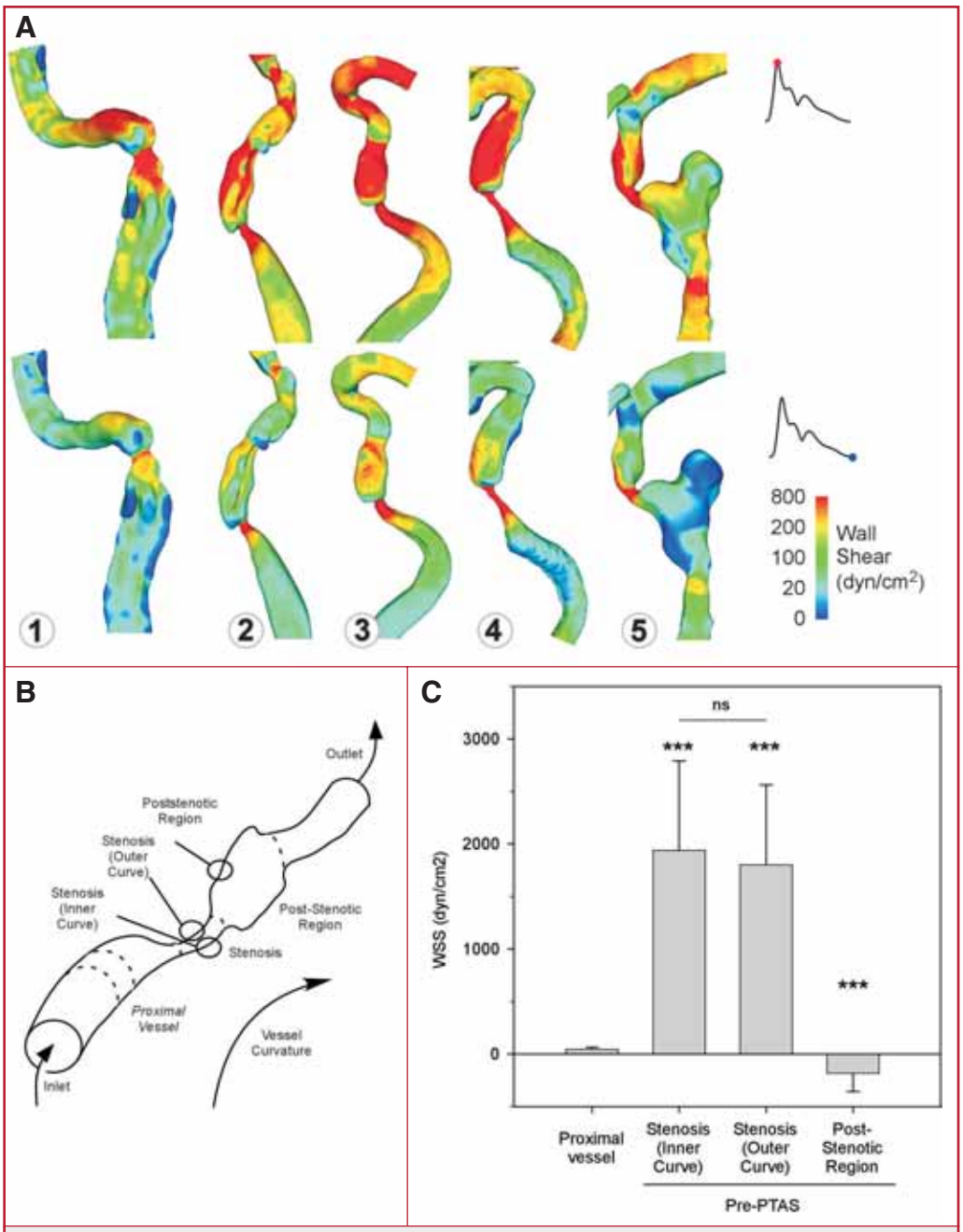


FIGURE 2. **A**, *contour plots of the wall shear stress (WSS) magnitude during peak systole* (upper panel) *and end diastole* (lower panel). Numbers *reflect the numbering of the cases in* Table 1. **B**, *schematic illustration of intracranial vessel and associated stenosis indicating the regions where directional WSS magnitude was averaged both spatially and temporally to derive the composite analysis.* **C**, *bar graph showing the time-averaged directional magnitude of the antegrade WSS values at the healthy proximal vessel segment upstream of the stenosis, at the stenosis itself (inner and outer curves), and at the maximal expansion of the poststenotic region (WSS encountered here has a retrograde direction). Values are mean ± standard deviation.*

The three-dimensional computational meshes of the vessels before PTAS were divided into four regions of interest: a ring segment on the healthy proximal vessel, regions on the inner

and outer sides of the stenosis facing toward and away from the local curvature of the vessel, respectively, and a region at the point of maximal dilatation in the PSR (*Fig. 2B*). Contralateral control vessels were similarly analyzed at the region corresponding to the location of the stenosis. These ROIs underwent spatial and temporal averaging of WSS directional magnitude during the cardiac pulse (*Fig. 2C*). Mean time-averaged WSS magnitude in the healthy upstream segment was 44 ± 19 dyn/cm^2, whereas it was 1939 ± 849 dyn/cm^2 on the inner curve and 1801 ± 761 dyn/cm^2 on the outer curve of the stenosis. In the PSR, the mean time-averaged WSS was −138 ± 47 dyn/cm^2, pointing in a retrograde direction to the bulk flow.

Cyclical Migration of Zones of Complex Shear Vectors

(see video at web site)

We analyzed the temporal evolution of the WSS vectors under pulsatile flow conditions over the course of the cardiac cycle. The emerging pattern revealed a highly complex dynamic process. *Figure 3A* illustrates the case of Patient 4 (*Video 2*): antegrade very high magnitude WSS vectors at the throat of the stenosis abruptly change direction to follow the recirculation of the blood flow that develops in the poststenotic dilatation. The location of the line separating these opposing shear directions (*line a*, *Fig. 3A*) shifts back and forth in sweeping motion over the course of the cardiac cycle, and is in this example more proximal during peak systole and more distal during the deceleration phase of the pulse. In contrast, another line demarcating the reattachment and realignment of WSS in the main flow direction in the distal PSR (*line b*, *Fig. 3A*) is more distal during peak-systole and becomes more proximal during diastole. A vortex of WSS vectors sweeps the distal portion of the PSR in a cyclic fashion (*circles c*, *Fig. 3A*).

Heterogeneous Time Profile of Shear Stress Distribution

Within the peristenotic region, evaluation of the time profile of WSS (*Fig. 3B*) reveals heterogeneous distributions within a small spatial region. Within the stenosis throat, very high WSS greater than 1000 dyn/cm^2 is maintained throughout the cardiac cycle, whereas in the immediate vicinity within the PSR, a zone of very rapidly fluctuating WSS occurs with alternating direction from 750 dyn/cm^2 to −200 dyn/cm^2 (negative denotes opposite direction) within less than 100 milliseconds. This phenomenon of rapidly oscillating WSS with alternating direction was further characterized by examining the temporal evolution of axial WSS along a cutline through the stenosis throat (X-Y line) (*Fig. 3C*; *Video 1*). The WSS profiles reveal a steady rise in WSS as one progresses through the throat of the stenosis, reaching greater than 6000 dyn/cm^2 at peak systole, followed by sharp reversal as one enters the PSR (*green arrows, Fig. 3C*). However, examination of the junction between the distal stenosis and proximal PSR reveals a focal zone (~1–2 mm long) of dynamic shear reversal in all lesions, which is exposed to extreme directional changes of nearly ±1000 dyn/cm^2 in the short time between peak systole and deceleration phases of the cardiac cycle (*green arrows*, *Fig. 3C*). These findings were confirmed in the remaining four lesions (*Fig. 3, D* and *E*). Plotting maximal difference of WSS against the time interval between the WSS extremes in this zone (WSS between the *green arrows* in *Fig. 3, C* and *E*) shows rapid change between −2590 dyn/cm^2 and 2990 dyn/cm^2 occurring over a short period (0.05–0.1 s). Both positive and negative WSS differences were noted (*Fig. 3F*).

Changes of WSS after PTAS

(see video at web site)

WSS vector direction in the poststenotic dilatation of IS lesions presented here is skewed and even retrograde in areas that migrate over time (*Fig. 4A*; see also *Fig. 3, A* and *D*). PTAS restored alignment of the WSS in the direction of mean flow (*Fig. 4A*; *Video 3*). Although the direction of WSS forces after PTAS remains because of parent vessel tortuosity, the areas of retrograde WSS vectors are much smaller and confined to the residual stenosis distal to the stent in Patient 3 (*Fig. 4A*).

In the PSR, mean time-averaged WSS was pointing in a direction retrograde to the bulk flow (*Fig. 2C*) and significantly different from both antegrade value within the stenosis ($P < 0.00004$) and restored antegrade WSS after PTAS ($P < 0.006$) (*Fig. 4B*). Mean time-averaged WSS magnitude following PTAS decreased to 81 ± 20 dyn/cm^2, not significantly different from 116 ± 70 dyn/cm^2 in contralateral control vessels ($P = 0.39$) (*Fig. 4B*). Sampling axial WSS on two points on the stent and along a cutline demonstrated resolution of the oscillating dynamic zone of shear reversal after PTAS (*Fig. 4C*).

OSI (25) is a normalized index that identifies regions undergoing relatively increased changes of WSS direction compared with the temporal average. *Figure 5* depicts the spectrum of OSI distribution for all cases, with regions of increased OSI corresponding to regions of rapid WSS directional changes (compare with *Fig. 3, A* and *D*).

Areas of increased OSI disappear after PTAS (*Fig. 5*), with small spots mostly proximal (*Fig. 5*, *Post-PTAS*, Patient 4) and distal to the stent (*Fig. 5*, *Post-PTAS*, Patient 2 and Patient 5) remaining. Patient 5 is more complex because of the associated aneurysm (*Fig. 5*, *Post-PTAS*, Patient 5).

DISCUSSION

Situated at the interface between blood flow and the vessel wall, the EC serves as the principal sensor of mechanical forces exerted by the blood flow on the vessel wall. EC phenotype and cellular function are tightly coupled to the local hemodynamic shear forces transmitted from the bloodstream (16, 23, 33–35). The spectrum of WSS changes in time and space in patient-based real stenotic intracranial geometries has not been described before. Intracranial atherosclerotic disease is associated with persistent neurological symptoms and stroke despite maximal medical therapy resulting from embolic events and hemodynamic insufficiency. Although PTAS has emerged as a possible treatment option for many types of lesions (30, 39), ongoing contro-

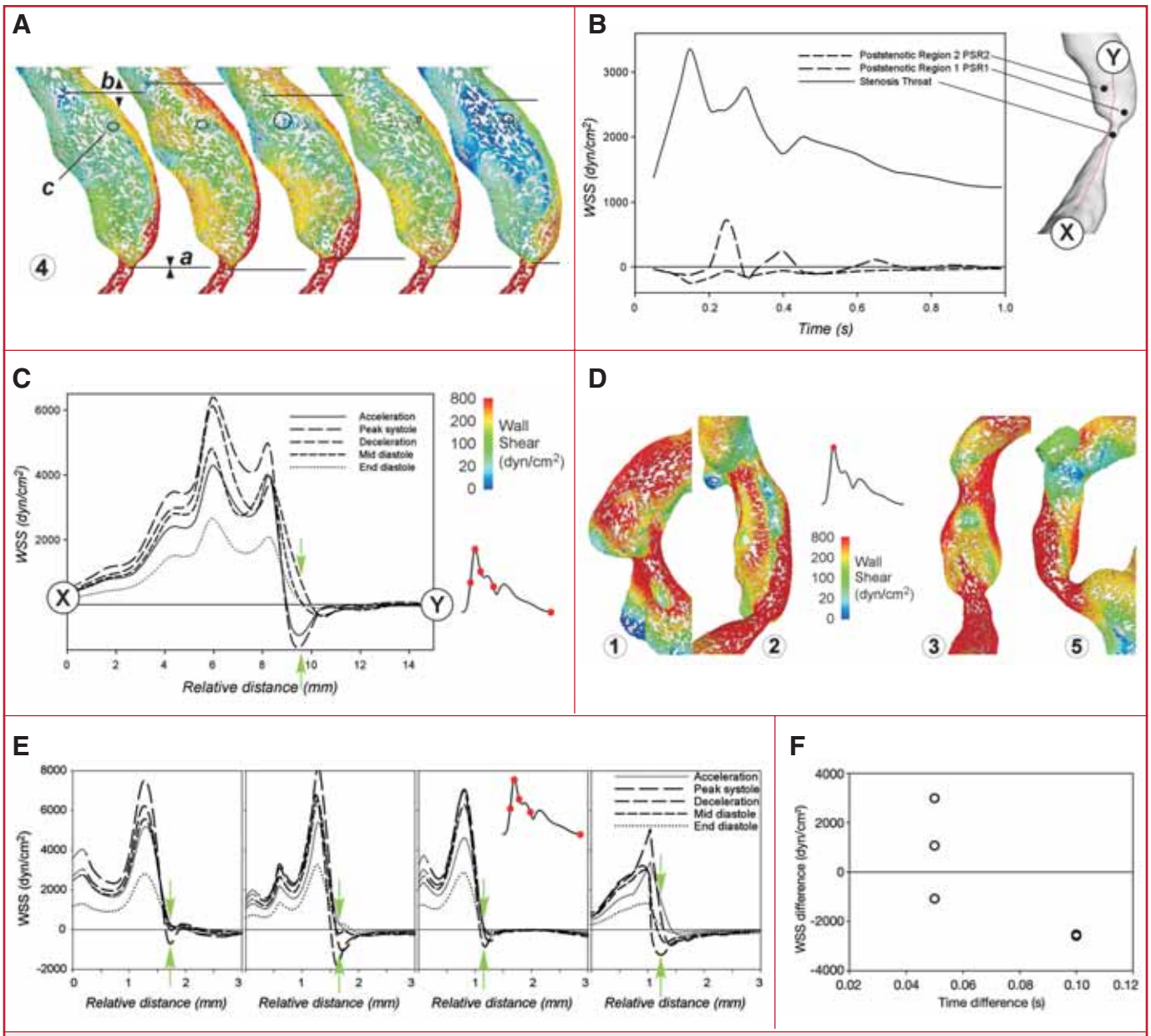


FIGURE 3. **A**, *Patient 4. Example detailing the temporal evolution of the instantaneous WSS vectors at the stenosis and poststenotic region during the cardiac cycle* (red points *on pulse wave).* Black lines a *and* b *demonstrate the stepwise changes of the location of the zone of shear reversal at the throat of the stenosis* (a) *and a reattachment line in the poststenotic region* (b). *A WSS vortex is outlined* (circles, c) *at the wall as it migrates in a cyclic fashion during the cardiac cycle.* **B**, *axial WSS magnitude during the cardiac cycle for three points at the throat of the stenosis and in the poststenotic region.* **C**, *axial WSS magnitude along the line between points* X *and* Y *(see schematic to the* right*) during five points of the cardiac cycle.* Green arrows *demarcate the region of shear direction reversal during cardiac cycle. Instantaneous WSS vectors at peak systole* (**D**) *and axial directional WSS magnitude along an X-Y cutline on the surface* (**E**) *in Patients 1, 2, 3, and 5.* **F**, *maximal difference of the WSS magnitude at the points indicated by* green arrows *in* **C** *and* **E**, *plotted against the time interval between the maximum and minimum WSS at that point.*

versy remains with respect to its role versus medical antiplatelet and anticoagulant therapy (10, 12). We set out to use high-resolution data sets obtained from three-dimensional rotational angiography combined with a robust computational approach to study the pattern of WSS in stenosed intracranial vessels and compare it with the WSS distributions found after PTAS. More frequently, available magnetic resonance imaging data that have been used to model flow in carotid bifurcations (6, 7) reproduce

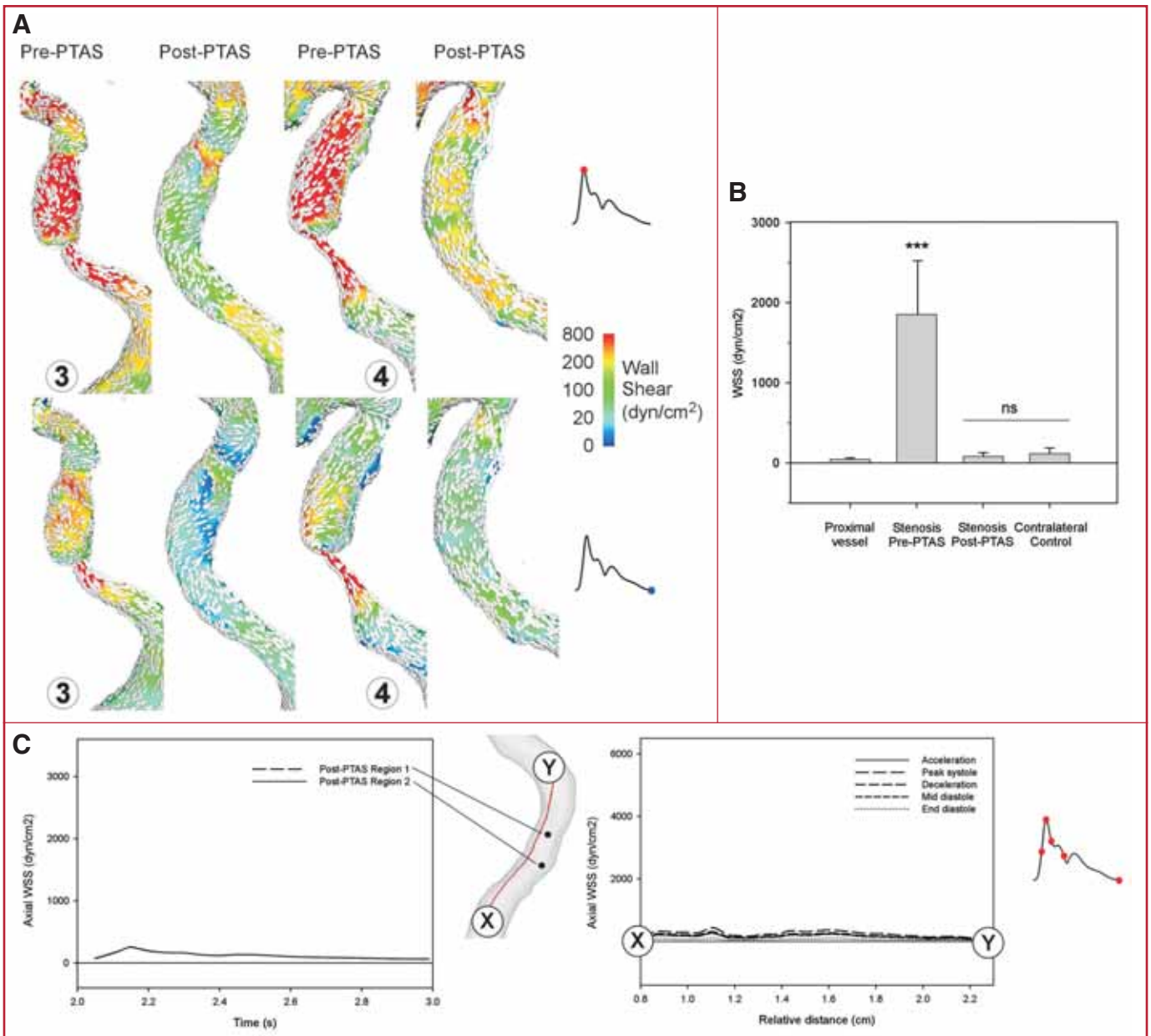


FIGURE 4. **A**, *contour plot of WSS in two representative intracranial stenosis lesions (Patients 3 and 4) overlaid with* arrowheads *to indicate the direction of the local WSS vector, during peak systole* (upper panel) *and end diastole* (lower panel), *Pre-PTAS and Post-PTAS.* **B**, *bar graph showing the time-averaged directional magnitude of the antegrade WSS values at the healthy proximal vessel segment upstream of the stenosis, at the stenosis itself, at the stenosis throat following PTAS and at the equivalent location in the contralateral vessel. Values are mean ± standard deviation.* **C**, *axial WSS magnitude during the cardiac cycle for two points at the throat of the stenosis after PTAS* (upper graph) *and axial WSS magnitude along the line between points* X *and* Y (*see schematic to the* right) *during five points of the cardiac cycle* (lower graph).

the anatomic detail of severe stenosis at the cranial base only poorly; thus, MRI is less suited for providing high-quality geometric data as the basis of the modeling approach.

The transition from laminar flow in a nonstenotic vessel to more complicated flow dynamics including recirculation and turbulent features in idealized stenosis has been investigated in the past (9, 20). These studies focused on the dynamics and behavior of the blood flow itself rather than on the changes the latter imparts on wall shear forces. In some cases, WSS was derived as an approximation from measurements of flow veloc-

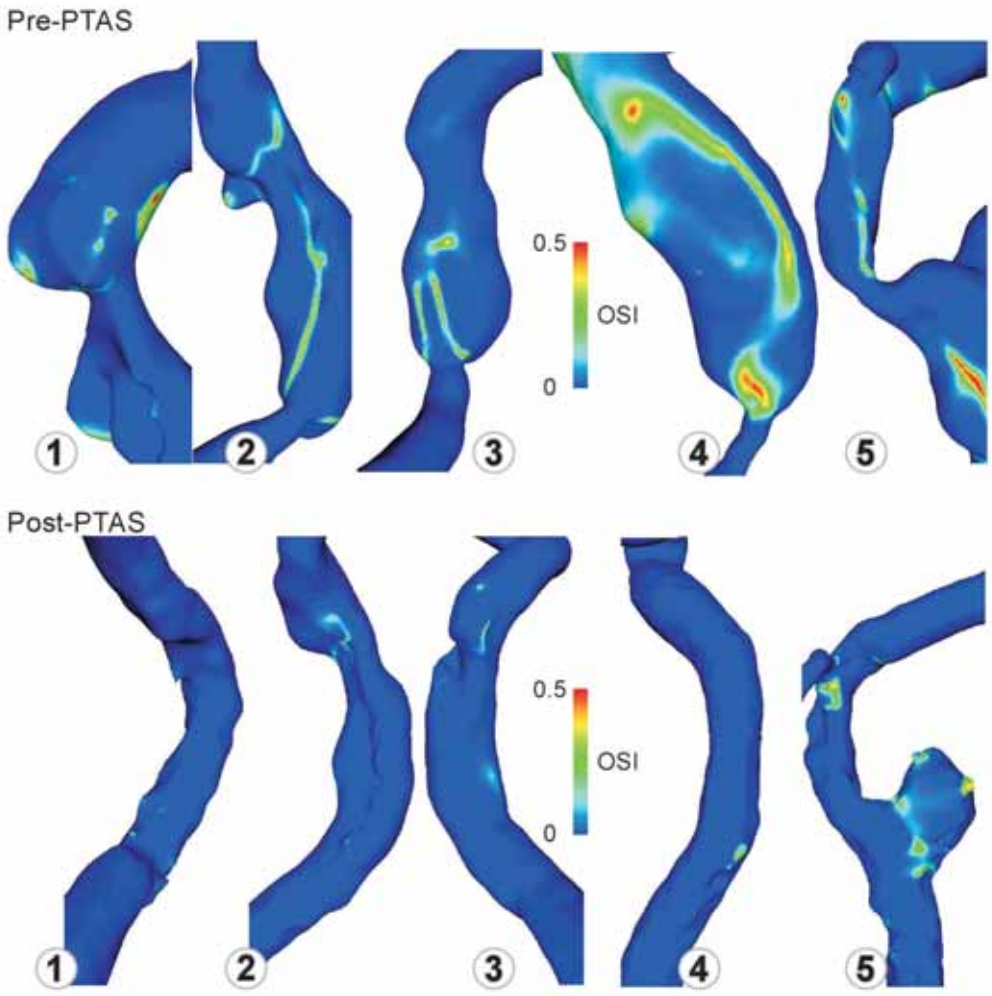


FIGURE 5. *Oscillatory shear index contour plots in all lesions before* (Pre-PTAS) *and after* (Post-PTAS) *PTAS.*

ity (2). Our baseline WSS of 40 dyn/cm^2 in the segment upstream of the stenosis is in agreement with the expected range of WSS in normal arteries. In contrast to in vitro studies of EC function that use low and high WSS values of around 4 and 25 dyn/cm^2, respectively, few studies have evaluated the effects of very high shear (>100–200 dyn/cm^2), with earlier studies by Fry reporting a denudation of the canine aortic EC layer after imposition of WSS above 379 dyn/cm^2 (17, 18). A more gradual experimental increase in WSS magnitude may allow the EC to develop the structural and functional adaptation needed to resist the even higher peak systolic WSS values (>1000 dyn/cm^2) seen in the 55 to 85% stenosis here.

WSS changes within the stenosis itself and the poststenotic region are highly complex and demonstrate significant variation throughout the cardiac cycle (*Fig. 2A*), with interindividual variation reflecting the spectrum of geometry of the stenoses in this study (*Figs. 2A* and *3, A* and *D*). Although a zone of flow separation with reversal of the shear direction with downstream realignment is common to all lesions in this series, its location was observed to shift over time in cyclic fashion in all lesions studied here (*Fig. 3A*). EC in vitro demonstrate a differential response to specific biomechanical forces with different types of mechanical stimuli transduced into distinct phenotypes (19). We showed that the shear forces in high-degree clinical IS lesions are altered in a fundamental way, providing a possible link between stenosed geometry and endothelial dysfunction in a vicious cycle of positive feedback. The zero WSS region identified between the distal stenosis and the PSR with convergent high WSS in opposing directions could have significant implications on local EC proliferation and turnover (15, 35, 38, 45).

Regions of elevated OSI have been associated in human aortas with the occurrence of sudanophilic lesions that are suggested to be precursors of atherosclerosis (11). In that study, regions of high OSI colocalized with low values of time-averaged shear, whereas high OSI such as is seen in the current work was adjacent to regions of high shear (shown during systole) (*Figs. 3* and *5*). PTAS caused the originally identified regions of elevated OSI to disappear (*Fig. 5*) and be replaced by smaller and less prominent regions of high OSI colocalized with the edges of the stented segment of the vessel. Increased OSI at the neck of the aneurysm in Patient 5 after PTAS is related to the associated aneurysmal dilatation, which was coiled after stent deployment (not shown).

CFD techniques have been used to study a healthy carotid bifurcation, using magnetic resonance angiography-mediated segmentation and modeling confirming the in vivo regional variation in EC phenotype in a disease-free carotid geometry (14). The much higher values of WSS in our study, which have not yet been replicated by in vitro models, offer a starting point for the molecular dissection of the EC mechanotransductive response to pathological hemodynamics within clinically significant stenosis. The link between high WSS gradients and increased permeability (38) and between high WSS values

greater than EC yield shear stress (17) may further point to a relationship between stenosis and exposure of blood to the subendothelial thrombogenic extracellular matrix; however, nonmechanical interactions between leukocytes, reactive oxygen species, and nitric oxide with the endothelial cells may also play an important role (13). Activation of platelets in the flow through stenoses (42) and aggregation on the vessel wall, potentially leading to thrombosis, are known to be regulated by shear forces. A dysfunctional EC surface with partially denuded areas or one with increased EC-EC gaps may provide a pathological surface that may influence platelet adhesion and aggregation.

Our current modeling technique has limitations: it assumes a rigid wall (32) and ignores plaque heterogeneity. It is accordingly less well suited for evaluating the stresses within potentially vulnerable plaque, as recently demonstrated (31), or the analysis of the viscoelastic and probably nonuniform spatial properties of an atherosclerotic vessel wall resulting from its complex geometry and heterogeneous material composition. Fluid-structure interaction techniques, which offer a potential solution by taking the deformation of the computational mesh by the prevailing pressure field iteratively into account, result in considerably larger computational requirements. Previous fluid-structure interaction analysis of a vessel stenosis used a smaller grid size of 32,000 cells (44) (compared with ~400,000 cells in this study), which would be insufficient to study the details of the flow in the poststenotic region. To our knowledge, it is unclear whether the assumption of an elastic wall would fundamentally alter the basic premise of our findings; a recent study of wall stress in an abdominal aortic aneurysm model showed a minimal difference between the solid stress and elastic wall (fluid-structure interaction) models (29).

We use a velocity waveform derived from healthy volunteers, which may not accurately represent the pulsatile waveform in patients with severe intracranial atherosclerotic disease. Although it would be desirable to have in vivo velocity data that can be coupled with the individual patient's geometry, such data were not available in the cases shown here. It is likely that an analysis using individual velocity waveforms would demonstrate potentially different results but that the qualitative features of our results, extremely elevated WSS values and oscillatory WSS patterns, would likely be maintained.

Non-Newtonian properties of blood were captured here using the Carreau-Yasuda model with the shear-thinning behavior as its dominant component, neglecting the viscoelastic properties (22). In another report on the model of a 25%, 50%, and 75% stenosis, the peak antegrade WSS measured at peak systolic flow on the wall at the throat of the stenosis is increased by 59, 5, and 6%, respectively, whereas no shifts in location of the reversal points of WSS and WSSG were observed when comparing the shear-thinning Carreau model with a constant viscosity model (42). Assuming a Newtonian fluid resulted in underestimation of both WSS and its gradient, consistent with previous studies showing non-Newtonian flows to exhibit a more blunt velocity profile with higher resulting wall forces (8).

The time-averaged maximum Reynolds number inside the simulated volume is below the limit usually assumed for the occurrence of turbulent flow, justifying our use of a laminar flow model. Models that account explicitly for the development of turbulent flow regimens are nevertheless of great interest, and other groups have used Reynolds-averaged techniques (such as the k-ε and k-ω model) (40, 49) that can model turbulence to study idealized axisymmetrical stenoses. These efforts have met with poor agreement of basic velocity and shear predictions with experimental results. More recently, direct numerical simulation has been used to achieve the same goal with better results (5).

Modeling the vessel geometry after PTAS using our approach does not explicitly reproduce the geometry of the stent struts. Although it would certainly be desirable to examine the CFD conditions immediately after PTAS and the changes caused by the stent struts, the current imaging modalities in clinical practice do not provide a high enough resolution to resolve the details of the stent geometry inside the vessel. We found that complexity of the reconstruction of the vessel geometry before and after PTAS was governed mostly by the artifacts caused by the proximity of the skull base; the presence of the stent played a much less dominant role.

CONCLUSION

The results of the current high-resolution CFD study predict a hemodynamic environment with extreme WSS values and rapid directional fluctuations within moderate to high-grade clinical intracranial stenoses and their respective poststenotic dilatations. These findings could serve as a conceptual framework for the continued progression of atherosclerosis in a positive-feedback model.

REFERENCES

1. Anonymous: Prognosis of patients with symptomatic vertebral or basilar artery stenosis. The Warfarin-Aspirin Symptomatic Intracranial Disease (WASID) Study Group. **Stroke** 29:1389–1392, 1998.
2. Ahmed SA, Giddens DP: Pulsatile poststenotic flow studies with laser Doppler anemometry. **J Biomech** 17:695–705, 1984.
3. Bagi Z, Frangos JA, Yeh JC, White CR, Kaley G, Koller A: PECAM-1 mediates NO-dependent dilation of arterioles to high temporal gradients of shear stress. **Arterioscler Thromb Vasc Biol** 25:1590–1595, 2005.
4. Bao X, Lu C, Frangos JA: Mechanism of temporal gradients in shear-induced ERK1/2 activation and proliferation in endothelial cells. **Am J Physiol** 281:H22–H29, 2001.
5. Beratlis N, Balaras E, Parvinian B, Kiger K: A numerical and experimental investigation of transitional pulsatile flow in a stenosed channel. **J Biomech Eng** 127:1147–1157, 2005.
6. Birchall D, Zaman A, Hacker J, Davies G, Mendelow D: Analysis of haemodynamic disturbance in the atherosclerotic carotid artery using computational fluid dynamics. **Eur Radiol** 16:1074–1083, 2006.
7. Botnar R, Rappitsch G, Scheidegger MB, Liepsch D, Perktold K, Boesiger P: Hemodynamics in the carotid artery bifurcation: A comparison between numerical simulations and in vitro MRI measurements. **J Biomech** 33:137–144, 2000.
8. Buchanan JR Jr, Kleinstreuer C, Comer JK: Rheological effects on pulsatile hemodynamics in a stenosed tube. **Computers Fluids** 29:695–724, 2000.

9. Cassanova RA, Giddens DP: Disorder distal to modeled stenoses in steady and pulsatile flow. **J Biomech** 11:441–453, 1978.
10. Chimowitz MI: Angioplasty or stenting is not appropriate as first-line treatment of intracranial stenosis. **Arch Neurol** 58:1690–1692, 2001.
11. Cornhill JF, Herderick EE, Stary HC: Topography of human aortic sudanophilic lesions. **Monogr Atheroscler** 15:13–19, 1990.
12. Cruz-Flores S, Diamond AL: Angioplasty for intracranial artery stenosis. **Cochrane Database Syst Rev** 3:CD004133, 2006.
13. Cunningham KS, Gotlieb AI: The role of shear stress in the pathogenesis of atherosclerosis. **Lab Invest** 85:9–23, 2005.
14. Dai G, Kaazempur-Mofrad MR, Natarajan S, Zhang Y, Vaughn S, Blackman BR, Kamm RD, Garcia-Cardeña G, Gimbrone MA Jr: Distinct endothelial phenotypes evoked by arterial waveforms derived from atherosclerosis-susceptible and -resistant regions of human vasculature. **Proc Natl Acad Sci USA** 101:14871–14876, 2004.
15. DePaola N, Davies PF, Pritchard WF Jr, Florez L, Harbeck N, Polacek DC: Spatial and temporal regulation of gap junction connexin43 in vascular endothelial cells exposed to controlled disturbed flows in vitro. **Proc Natl Acad Sci USA** 96:3154–3159, 1999.
16. DePaola N, Gimbrone MA Jr, Davies PF, Dewey CF Jr: Vascular endothelium responds to fluid shear stress gradients. **Arterioscler Thromb** 12:1254–1257, 1992.
17. Fry DL: Acute vascular endothelial changes associated with increased blood velocity gradients. **Circ Res** 22:165–197, 1968.
18. Fry DL: Certain histological and chemical responses of the vascular interface to acutely induced mechanical stress in the aorta of the dog. **Circ Res** 24:93–108, 1969.
19. Garcia-Cardeña G, Comander J, Anderson KR, Blackman BR, Gimbrone MA Jr: Biomechanical activation of vascular endothelium as a determinant of its functional phenotype. **Proc Natl Acad Sci USA** 98:4478–4485, 2001.
20. Giddens DP, Mabon RF, Cassanova RA: Measurements of disordered flows distal to subtotal vascular stenoses in the thoracic aortas of dogs. **Circ Res** 39:112–119, 1976.
21. Giddens DP, Zarins CK, Glagov S: The role of fluid mechanics in the localization and detection of atherosclerosis. **J Biomech Eng** 115:588–594, 1993.
22. Gijsen FJ, van de Vosse FN, Janssen JD: The influence of the non-Newtonian properties of blood on the flow in large arteries: Steady flow in a carotid bifurcation model. **J Biomech** 32:601–608, 1999.
23. Gimbrone MA Jr, Resnick N, Nagel T, Khachigian LM, Collins T, Topper JN: Hemodynamics, endothelial gene expression, and atherogenesis. **Ann N Y Acad Sci** 811:1–11, 1997.
24. Hsiai TK, Cho SK, Wong PK, Ing M, Salazar A, Sevanian A, Navab M, Demer LL, Ho CM: Monocyte recruitment to endothelial cells in response to oscillatory shear stress. **FASEB J** 17:1648–1657, 2003.
25. Hyun S, Kleinstreuer C, Longest PW, Chen C: Particle-hemodynamics simulations and design options for surgical reconstruction of diseased carotid artery bifurcations. **J Biomech Eng** 126:188–195, 2004.
26. Kasner SE, Chimowitz MI, Lynn MJ, Howlett-Smith H, Stern BJ, Hertzberg VS, Frankel MR, Levine SR, Chaturvedi S, Benesch CG, Sila CA, Jovin TG, Romano JG, Cloft HJ; Warfarin Aspirin Symptomatic Intracranial Disease Trial Investigators: Predictors of ischemic stroke in the territory of a symptomatic intracranial arterial stenosis. **Circulation** 113:555–563, 2006.
27. Kasner SE, Lynn MJ, Chimowitz MI, Frankel MR, Howlett-Smith H, Hertzberg VS, Chaturvedi S, Levine SR, Stern BJ, Benesch CG, Jovin TG, Sila CA, Romano JG; Warfarin Aspirin Symptomatic Intracranial Disease (WASID) Trial Investigators: Warfarin vs aspirin for symptomatic intracranial stenosis: Subgroup analyses from WASID. **Neurology** 67:1275–1278, 2006.
28. Köhler U, Marshall I, Robertson MB, Long Q, Xu XY, Hoskins PR: MRI measurement of wall shear stress vectors in bifurcation models and comparison with CFD predictions. **J Magn Reson Imaging** 14:563–573, 2001.
29. Leung JH, Wright AR, Cheshire N, Crane J, Thom SA, Hughes AD, Xu Y: Fluid structure interaction of patient specific abdominal aortic aneurysms: A comparison with solid stress models. **Biomed Eng Online** 5:33, 2006.
30. Levy EI, Hanel RA, Bendok BR, Boulos AS, Hartney ML, Guterman LR, Qureshi AI, Hopkins LN: Staged stent-assisted angioplasty for symptomatic intracranial vertebrobasilar artery stenosis. **J Neurosurg** 97:1294–1301, 2002.
31. Li ZY, Howarth SP, Tang T, Gillard JH: How critical is fibrous cap thickness to carotid plaque stability? A flow-plaque interaction model. **Stroke** 37:1195–1199, 2006.
32. Liu Y, Lai Y, Nagaraj A, Kane B, Hamilton A, Greene R, McPherson DD, Chandran KB: Pulsatile flow simulation in arterial vascular segments with intravascular ultrasound images. **Med Eng Phys** 23:583–595, 2001.
33. Malek AM, Alper SL, Izumo S: Hemodynamic shear stress and its role in atherosclerosis. **JAMA** 282:2035–2042, 1999.
34. Malek AM, Izumo S, Alper SL: Modulation by pathophysiological stimuli of the shear stress-induced up-regulation of endothelial nitric oxide synthase expression in endothelial cells. **Neurosurgery** 45:334–345, 1999.
35. Nagel T, Resnick N, Dewey CF Jr, Gimbrone MA Jr: Vascular endothelial cells respond to spatial gradients in fluid shear stress by enhanced activation of transcription factors. **Arterioscler Thromb Vasc Biol** 19:1825–1834, 1999.
36. NASCET: Beneficial effect of carotid endarterectomy in symptomatic patients with high-grade carotid stenosis. North American Symptomatic Carotid Endarterectomy Trial Collaborators. **N Engl J Med** 325:445–453, 1991.
37. Ovbiagele B, Saver JL, Lynn MJ, Chimowitz M; WASID Study Group: Impact of metabolic syndrome on prognosis of symptomatic intracranial atherostenosis. **Neurology** 66:1344–1349, 2006.
38. Phelps JE, DePaola N: Spatial variations in endothelial barrier function in disturbed flows in vitro. **Am J Physiol** 278:H469–H476, 2000.
39. Rasmussen PA: Transluminal stent-assisted angioplasty of the intracranial vertebrobasilar system for medically refractory, posterior circulation ischemia: Early results. **Neurosurgery** 49:1489–1490, 2001.
40. Ryval J, Straatman AG, Steinman DA: Two-equation turbulence modeling of pulsatile flow in a stenosed tube. **J Biomech Eng** 126:625–635, 2004.
41. Schirmer CM, Malek AM: Prediction of complex flow patterns in intracranial atherosclerotic disease using computational fluid dynamics. **Neurosurgery** 61:842–852, 2007.
42. Schirmer CM, Malek AM: Wall shear stress gradient analysis within an idealized stenosis using non-Newtonian flow. **Neurosurgery** 61:853–864, 2007.
43. Stroud JS, Berger SA, Saloner D: Numerical analysis of flow through a severely stenotic carotid artery bifurcation. **J Biomech Eng** 124:9–20, 2002.
44. Tang D, Yang C, Kobayashi S, Ku DN: Steady flow and wall compression in stenotic arteries: A three-dimensional thick-wall model with fluid-wall interactions. **J Biomech Eng** 123:548–557, 2001.
45. Tardy Y, Resnick N, Nagel T, Gimbrone MA Jr, Dewey CF Jr: Shear stress gradients remodel endothelial monolayers in vitro via a cell proliferation-migration-loss cycle. **Arterioscler Thromb Vasc Biol** 17:3102–3106, 1997.
46. Thomas JB, Milner JS, Rutt BK, Steinman DA: Reproducibility of image-based computational fluid dynamics models of the human carotid bifurcation. **Ann Biomed Eng** 31:132–141, 2003.
47. Thurston GB: Frequency and shear rate dependence of viscoelasticity of human blood. **Biorheology** 10:375–381, 1973.
48. Thurston GB: Rheological parameters for the viscosity viscoelasticity and thixotropy of blood. **Biorheology** 16:149–162, 1979.
49. Varghese SS, Frankel SH: Numerical modeling of pulsatile turbulent flow in stenotic vessels. **J Biomech Eng** 125:445–460, 2003.
50. White CR, Haidekker M, Bao X, Frangos JA: Temporal gradients in shear, but not spatial gradients, stimulate endothelial cell proliferation. **Circulation** 103:2508–2513, 2001.

Acknowledgment

This work was funded in part by a grant from the Cam Neely Foundation to the Boston Institute of Neurosurgery at Tufts Medical Center.

COMMENTS

Schirmer and Malek analyzed luminal patterns of wall shear stress (WSS) within intracranial atherosclerotic lesions undergoing percutaneous angioplasty and stenting (PTAS) using computational fluid dynamics methods. Their previous article described details of the methods, and in this article they adopted their methods in five patients with

intracranial atherosclerotic lesions and showed interesting spatial and temporal changes in WSS patterns before and after PTAS. WSS within the stenosis reached high average shear magnitudes with rapidly reversing direction to oscillating low values in the recirculation zone and WSS vectors revealed complex dynamic directional and amplitude oscillations during the cardiac cycle; PTAS normalized such extreme WSS magnitudes and variations. Dynamic changes in WSS contribute to alterations in endothelial functions and may lead to progression in various vascular diseases including cerebral aneurysms. Better understanding of the effects of focal mechanical environments on vessel walls seems to be helpful in analyzing molecular mechanisms of hemodynamic stress to luminal endothelium. Further analysis on the basis of each patient's data may be helpful to individualize treatment modalities in cerebrovascular diseases.

Kazuhiko Nozaki
Shiga, Japan

With the continuing evolution of endovascular neurosurgical therapies, it is crucial to have a better understanding of endoluminal factors in disease pathophysiology and treatment effects as reflected by flow within the blood vessels as well as shear stress in their walls. Although computational fluid dynamics analyses have been available for some time with this elegant computer-based model, the authors analyzed factors in a small patient group with intracranial atherosclerotic disease who were undergoing angioplasty and stenting. What they found were complex shear stresses across the diseased segments compared with those in healthy arteries. This early study surely indicates that many more similar studies on larger number of patients with differing intravascular pathological conditions are needed as we proceed to become evermore adventurous in our endoluminal therapies.

Schirmer and Malek used computational fluid dynamics methods to analyze luminal patterns of WSS, a known critical modulator of endothelial function in patients undergoing PTAS. WSS was analyzed spatiotemporally in five intracranial atherosclerotic disease lesions before and after PTAS. WSS vectors revealed complex dynamic directional and amplitude oscillations not seen in healthy segments with time-dependent convergence and divergence strips sweeping back and forth across the lesion during the cardiac cycle.

Neal F. Kassell
Charlottesville, Virginia



The Blue Room *by Picasso, 1901. Oil on canvas. Courtesy of the Phillips Collection, Washington, D.C.*